nature communications

Article

https://doi.org/10.1038/s41467-026-75886-w

Electrically driven inverse metamagnetic transition in $Sm_{1-x}Sr_xMnO_3$

Received: 7 November 2025

Accepted: 14 July 2026

Published online: 25 July 2026

Check for updates

Suryakanta Mondal[1,8], Vinod Kumar[1,8], Sourav Chowdhury[2], Akshat Godha[1], Arup Kumar Mandal[1], Wan-Sheng Tang[3], Alan Kalitsov[4], Ashish Omar[1], Subhajit Nandy[2], Jayjit Kumar Dey[2], Gyanendra Panchal[2], Surendra Kumar Makineni[1], Julia Mundy[5], Yu-Hui Tang[3], Sasikanth Manipatruni[4], Manuel Bibes[6], Mark Blamire[7] & Bhagwati Prasad[1]

Electrical control of magnetic order remains one of the fundamental pursuits in condensed matter physics and spintronics, offering transformative potential for energy-efficient, high-density information technologies. While current-induced switching via spin-transfer and spin-orbit torques is well established in ferromagnets, electrically driving a transition between distinct magnetic phases, specifically from a ferromagnetic to an antiferromagnetic state, remains largely unexplored experimentally. Here, we demonstrate a reversible, electrically-driven inverse metamagnetic transition in an epitaxial thin film of the correlated manganite $Sm_{1-x}Sr_xMnO_3$. Above a critical current threshold, the system abruptly switches from a low-resistance ferromagnetic state to a high-resistance antiferromagnetic-like phase. We exploit this phenomenon in nanoscale (250 × 250 nm^2) spin-filter tunnel junctions based on $LaNiO_3/Sm_{0.75}Sr_{0.25}MnO_3/SrTiO_3/La_{0.7}Sr_{0.3}MnO_3$ heterostructures, realizing robust, bistable resistance switching with unconventional magnetoresistance exceeding 200 %, tunable by current, temperature, and magnetic field. These findings open a phase-transition-based route for electrically driven spintronic devices beyond conventional torque-based strategies.

The electric control of magnetic order lies at the core of efforts to develop energy-efficient and non-volatile information technologies[1–4]. As conventional charge-based electronics face fundamental scaling and power limitations[5] spin-based approaches have emerged as promising alternatives, leveraging the electron's spin degree of freedom for information storage and processing[6]. Among various material platforms, transition-metal oxides offer a compelling playground for spintronics, owing to their strong electronic correlations, tunable magnetic properties, and compatibility with high-quality epitaxial growth[7–11].

In correlated oxide systems, one particularly intriguing phenomenon is the metamagnetic phase transition, in which a material undergoes an abrupt transformation from a non-ferromagnetic state, such as paramagnetic or antiferromagnetic, to a ferromagnetic one under an external perturbation[12]. Metamagnetic transitions are typically sensitive to parameters such as magnetic field, strain, temperature, and carrier concentration, and often result from a delicate balance between competing magnetic ground states[12–15]. Kuwahara et al.[16] demonstrated magnetic-field-induced metamagnetic switching in

[1]Department of Materials Engineering, Indian Institute of Science, Bengaluru, KA, India. [2]Deutsches Elektronen-Synchrotron, DESY Notkestrabe 85, Hamburg, Germany. [3]Department of Physics, National Central University, Jung-Li, Taiwan. [4]Kepler Computing, Inc., 1200 5th Street, Berkeley, California, USA. [5]Department of Physics, Harvard University, Cambridge, USA. [6]Laboratoire Albert Fert, CNRS, Thales, Université Paris-Scalay, Palaiseau, France. [7]Department of Materials Science and Metallurgy, University of Cambridge, 27 Charles Babbage Road, Cambridge, UK. [8]These authors contributed equally: Suryakanta Mondal, Vinod Kumar. e-mail: bpjoshi@iisc.ac.in

$Nd_{0.5}Sr_{0.5}MnO_3$, highlighting the competition between double exchange and charge/orbital ordering. In $Ca_3Ru_2O_7$, chiral spin textures emerge from a magnetic-field-driven mixed state of ferromagnetic and antiferromagnetic phases, originating from an antiferromagnetic ground state and accompanied by spin twisting induced by the Dzyaloshinskii-Moriya interaction[17]. Other examples include magnetic-field-induced transitions in $Pr_2Zr_2O_7$ at sub-millikelvin temperatures[18] and optically induced phase changes in FeRh using ultrafast laser pulses[19]. Strain-coupled heterostructures, such as FeRh/$BaTiO_3$[2], and FeRh/PMN-PT[20], have also demonstrated electric-field-mediated control of metamagnetism via magnetoelectric coupling.

Despite these advances, most demonstrations of metamagnetism have relied on external magnetic fields[2], strain[16] or optical excitation[14], approaches that limit device scalability and on-chip integration. In contrast, electrical current offers a highly localized and energy-efficient pathway to control magnetic states. Current-driven switching mechanisms studied thus far, such as spin-transfer torque (STT)[21] and spin-orbit torque (SOT)[22], typically operate within a fixed ferromagnetic phase, enabling magnetization reversal without altering the underlying magnetic order[23,24]. Yet an energy-efficient, current-driven switching scheme remains unrealized. A current-induced transition from a ferromagnetic (FM) to an antiferromagnetic (AFM) phase, termed an inverse metamagnetic transition[25,26], remains largely unexplored. Realizing such a transition would expand the operating principles of spintronic devices, enabling electrically reconfigurable magnetic phases with zero net magnetization, enhanced thermal stability, and minimal stray fields.

Here, we report the experimental realization of an electrically driven inverse metamagnetic transition in an epitaxial thin film of the correlated manganite $Sm_{1-x}Sr_xMnO_3$. Building on this result, we incorporate a ferromagnetic insulating (FI) phase of $Sm_{1-x}Sr_xMnO_3$ ($x \approx 0.25$) into spin-filter tunnel junctions (SFTJs) to investigate this transition in a functional device architecture. Unlike conventional STT or SOT devices, which toggle spin polarization within a single FM phase, SFTJs utilize a magnetic tunnel barrier to generate spin-polarized currents via exchange-split conduction bands. Magnetic-field-induced metamagnetic transitions have previously been realized in SFTJs based on EuSe[27], and strong bias-dependent magnetoresistance has been reported in manganite-based junctions[28]. However, an electrically driven inverse metamagnetic transition in such devices remains to be systematically explored. Our results reveal a sharp and reversible transition to an AFM, high-resistance state under applied current, distinct from conventional STT and SOT mechanisms. This work establishes a framework for current-driven magnetic phase control in oxide heterostructures, laying the foundation for a class of energy-efficient spintronic devices that exploit the complex phase landscape of correlated oxides.

Results

To investigate current-driven magnetic switching in a correlated oxide system, we synthesized a high-quality epitaxial thin film of the $Sm_{1-x}Sr_xMnO_3$ ($x \approx 0.4$) on $SrTiO_3$ (STO) (001) substrate using the pulsed laser deposition (PLD) technique (see "Methods"). The crystalline quality and epitaxial nature of the films were confirmed by X-ray diffraction (XRD), with reciprocal space mapping (RSM) revealing relaxed, lattice-matched growth of the SSMO film on STO substrate (Fig. S1). Temperature-dependent resistance measurements revealed a metallic transport behavior at low temperatures (Fig. S2a). Additionally, the magnetization data confirmed a ferromagnetic ground state below the Curie temperature $T_C \sim 100$ K (Fig. S2b, c).

We next investigated the electrical transport response of the SSMO thin film under applied current in a four-probe configuration to examine the emergence of nonequilibrium magnetic phenomena. As shown in Fig. 1a, the longitudinal resistance (R) of the film measured at 5 K exhibits an abrupt, step-like increase at a threshold current (I_C) of approximately 3.5 mA, indicating a transition from a low-resistance to a high-resistance state. Notably, the threshold current increases systematically with the application of an increasing external magnetic field (inset, Fig. 1a), suggesting a strong interplay between the underlying magnetic order and current-driven transport.

To further elucidate this behavior, we performed magnetoresistance (MR) measurements at various current levels. At currents ≤3 mA, the film exhibits a conventional negative MR response (Fig. 1b), consistent with spin-dependent scattering in the ferromagnetic metallic phase[29]. However, at higher currents ($I \geq I_c$), an unconventional and hysteretic resistance switching emerges. As the magnetic field is swept from positive values toward zero, the resistance abruptly switches from a low- to high-resistance state. The low-resistance state is recovered only upon application of a large negative magnetic field, resulting in a pronounced hysteresis loop (Fig. 1b). This bistable switching persists over multiple field cycles and becomes increasingly prominent with higher applied currents.

To directly probe the evolution of magnetic order under applied current, we performed X-ray magnetic circular dichroism (XMCD) and X-ray linear dichroism (XLD) measurements at the Mn $L_{3,2}$ absorption edges at 25 K under a 1 T magnetic field, as shown in Fig. 1c, d, respectively (also see Fig. S3). At zero and low currents (≤ 1 mA), a strong XMCD signal is observed, consistent with a robust ferromagnetic ground state in the SSMO thin film (Fig. 1c). Strikingly, the XMCD signal vanishes upon increasing the applied current to 5 mA, indicating a complete suppression of long-range ferromagnetic order beyond the critical current threshold (Fig. 1c). Simultaneously, XLD measurements reveal a pronounced shift in orbital occupancy from predominantly in-plane ($3d_{x^2-y^2}$) character at zero and low current (≤ 1 mA) to out-of-plane ($3d_{3z^2-r^2}$) character at higher currents (Fig. 1d)[30–34] (See "Methods" for a detailed analysis). Charge-transfer multiplet calculations of the Mn $L_{3,2}$ -edges XLD spectra within a D_{4h} crystal field framework reproduce the characteristic spectral signatures of these two orbital-polarization states and support this interpretation (see Supplementary Information, Fig. S11 and Section A). Notably, Aruta et al.[35] demonstrated that in ultrathin films of ferromagnetic LSMO, an antiferromagnetic insulating (AFI) phase can be stabilized via interfacial rearrangement of Mn 3 d orbitals. The orbital reconfiguration reflects a strong coupling between spin and orbital degrees of freedom and suggests that the current-induced suppression of ferromagnetism is accompanied by a reconfiguration of the electronic structure from the in-plane ($3d_{x^2-y^2}$) to out-of-plane ($3d_{3z^2-r^2}$) character. These findings indicate that the current suppresses the ferromagnetic state and drives the system toward an AFM-like phase, rather than a simple paramagnetic state caused by Joule heating, consistent with an orbital-driven inverse metamagnetic transition, as schematically illustrated in Fig. 1e[30,34,36].

Having established electrical control over FM metallic phases in $Sm_{0.6}Sr_{0.4}MnO_3$ thin film, we next sought to implement this mechanism in a functional tunnel device architecture. For this purpose, the Sr concentration was reduced to engineer a ferromagnetic insulating (FI) state at low temperatures, specifically in $Sm_{0.75}Sr_{0.25}MnO_3$ (SSMO-FI), enabling its use as a spin-filter tunnel barrier. This composition preserves the strong magnetic order required for spin-dependent tunneling while introducing the insulating behavior necessary for tunnel transport (see Fig. S4). Our objective was to exploit the intrinsic current-induced magnetic phase transition of SSMO-FI within a spin-filter tunnel junction (SFTJ) platform, thereby achieving electrical control of resistance states in a practical device configuration.

Epitaxial oxide heterostructures with the stack configuration $LaNiO_3$(LNO)/SSMO-FI/STO/$La_{0.7}Sr_{0.3}MnO_3$(LSMO) were fabricated for the development of SFTJ devices. The multilayer film was grown by PLD in an oxygen atmosphere on STO (001) substrate (see "Methods" section for details). Cross-sectional high-resolution scanning

https://doi.org/10.1038/s41467-026-75886-w

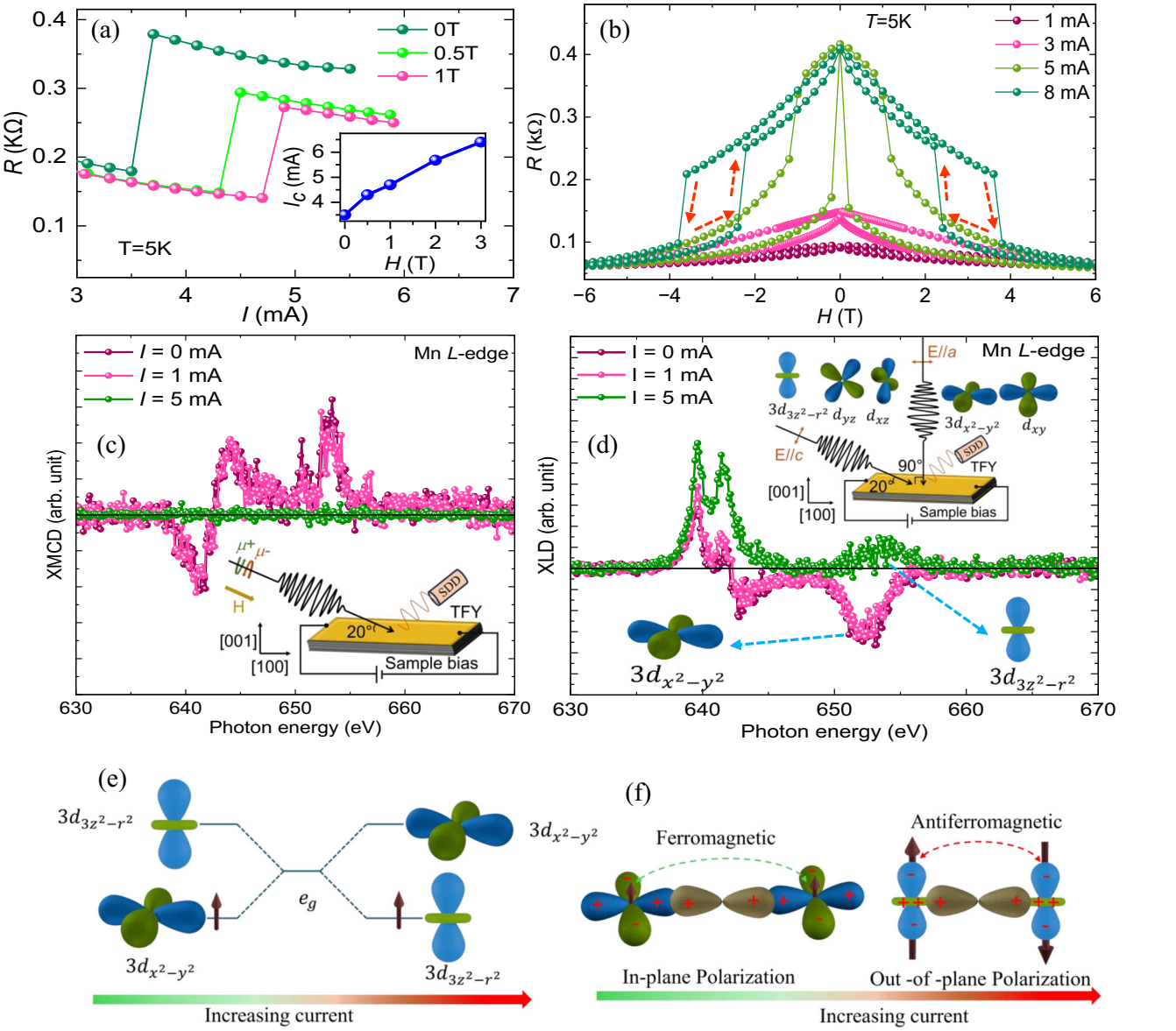

Fig. 1 | Current-induced resistance switching, magnetoresistance, and electric-bias-dependent XMCD/XLD measurements in SSMO thin film. a Resistance vs. current measured at 5 K under varying magnetic fields, showing abrupt current-induced switching correlated with field strength. **b** Magnetoresistance (MR) behavior at 5 K under different applied currents reveals unconventional, hysteretic switching above a critical current of ~3.5 mA. **c** XMCD spectra at the Mn $L_{3,2}$-edges under increasing current at 25 K; the XMCD signal vanishes at 5 mA, indicating suppression of ferromagnetism. **d** XLD spectra under varying current at 25 K show a transition from negative (in-plane $3d_{x^2-y^2}$) polarization at 0–1 mA to positive (out-of-plane $3d_{3z^2-r^2}$) polarization at 5 mA, as illustrated in the inset. XMCD and XLD spectra were measured in total fluorescence (TFY) mode using a silicon drift doctor (SDD). **e** Schematic illustration of current-driven orbital polarization switching from in-plane to out-of-plane (arrows represent electron spins). **f** Schematic representation of ferromagnetic to antiferromagnetic ordering, where broken green arrows indicate ferromagnetic alignment (parallel spins) and broken red arrows indicate antiferromagnetic alignment (antiparallel spins).

transmission electron microscopy (HR-STEM) imaging (Fig. 2a, b) reveals epitaxial, high crystallinity growth with atomically sharp interfaces and coherent multilayer stacking. The RSM data further confirms that the heterostructures remain nearly fully latticed matched to the STO (001) substrate, indicating minimal strain relaxation (Fig. S5). Elemental mapping via EDX (Fig. S6) shows abrupt interfaces with minimal interlayer diffusion, highlighting the precise control achieved during growth. Multilayer oxide films were patterned by photolithography into 4-μm-wide tracks with contact pads (Fig. 2c, top), narrowed to ~250 nm by focused ion beam nanomachining (Fig. 2c, middle/bottom), and finally formed into ~250 × 250 nm nanopillar tunnel junctions (Fig. 2d). Detailed fabrication procedures are provided in the "Methods" and elsewhere[28].

Figure 2e shows the resistance as a function of magnetic field for a representative SFTJ device with the stack configuration LNO (200 nm)/SSMO-FI (8.5 nm)/STO (1 nm)/LSMO (200 nm), where LSMO serves as the ferromagnetic bottom electrode, LNO is the non-magnetic top electrode, and the 1 nm STO layer acts as a magnetic decoupling layer between the SSMO-FI barrier and the LSMO electrode. At an applied bias current of −93 μA, the device exhibits a low resistance state under large positive magnetic fields, corresponding to the parallel alignment of the magnetizations in the SSMO-FI and LSMO layers. This results in enhanced preferential spin-polarized tunneling of electrons, as expected in conventional SFTJ operation[37–39]. However, as the magnetic field is reduced from high positive values, the resistance switches abruptly from a low to a high state at 0.24 T, despite the nominal

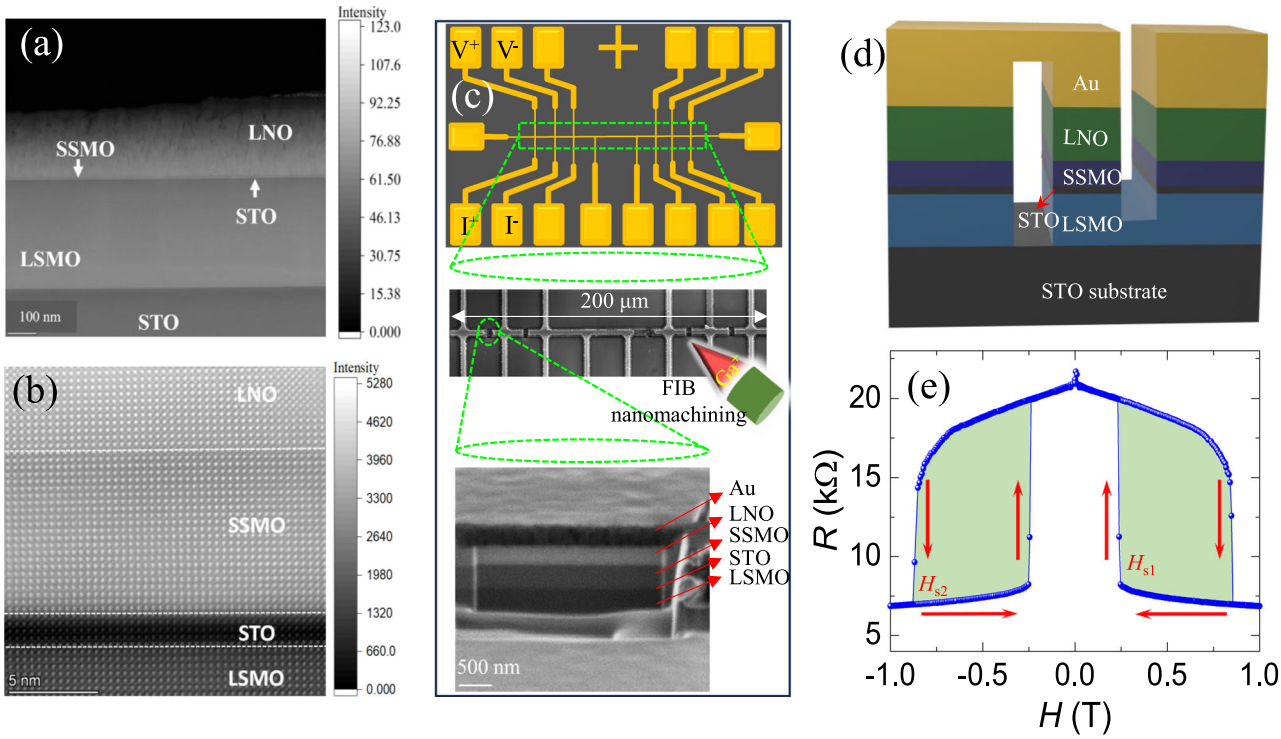

Fig. 2 | Epitaxial oxide heterostructures and SFTJ device fabrication and measurements. a Cross-sectional high-resolution TEM image showing the epitaxial growth of a $LaNiO_3$ (LNO)/$Sm_{0.75}Sr_{0.25}MnO_3$ (SSMO-FI)/$SrTiO_3$ (STO)/$La_{0.7}Sr_{0.3}MnO_3$ (LSMO) heterostructure on an STO (001) substrate. **b** High-resolution STEM image revealing atomically sharp interfaces between LNO, SSMO-FI, STO and LSMO layers. The color scale provided in figs (**a**, **b**) represents the intensity scale, ranging from black to white, corresponding to minimum to maximum intensity. **c** SFTJ device fabrication process: schematic of the patterned chip after photolithography (top), SEM image of the central chip region containing multiple SFTJ devices after FIB nanomachining (middle), and cross-sectional SEM image of a ~250nm-wide microstrip (bottom). **d** Schematic of the two-terminal nanopillar SFTJ device. **e** Magnetoresistance of a representative SFTJ device measured at 5 K with a fixed bias current of −93 μA. H_{S1} and H_{S2} mark the low-to-high and high-to-low resistance switching fields, respectively.

parallel configuration of the magnetic layers. Upon reversing the field direction, the resistance returns to a low state at a large negative field (−0.87 T). This hysteretic resistance switching is consistently observed over multiple magnetic field cycles. Importantly, this behavior deviates from the conventional model of spin-filter tunneling, where resistance changes are determined by the coercive fields of the magnetic layers and the exchange-splitting within the FI barrier[27,37,40]. In typical SFTJs, the resistance hysteresis mimics that of a pseudo-spin-valve, with switching tied to magnetization reversal in the electrode and barrier layer[41]. In contrast, for our devices, the resistance switching does not coincide with the coercive fields of either the SSMO-FI or LSMO layers (Fig. S4)-switching occurs before zero field and shows a pronounced dependence on the applied current (see Fig. 3). Notably, the magnetization reversal of the LSMO at low fields does not induce a significant resistance change, implying that in the high-resistance state, the SSMO-FI barrier is no longer ferromagnetic and lacks spin-split energy levels. These observations suggest that an applied current above the I_c destabilizes the FI states, leading to an AFM state and accordingly suppressing spin-selective tunneling. This is consistent with an inverse metamagnetic transition as inferred for the single film but now occurring within the operational tunnel device.

Figure 3a, b presents the *R-H* characteristics for different negative bias currents. At lower current levels, the device remains in a low resistance state across the entire magnetic field range, but upon increasing the bias to approximately − 80 μA, resistance switching emerges, corresponding to the conventional tunneling magnetoresistance (TMR) response of the SFTJ device. This behavior persists for the currents up to −87 μA, though the observed TMR ratio remains relatively modest (Fig. 3a), as commonly seen in SFTJ devices at low bias, with TMR typically increasing with bias magnitude[28]. Notably, upon further increasing the bias beyond a critical threshold of approximately −88 μA, the magnetoresistance response undergoes a qualitative change (Fig. 3b), exhibiting unconventional switching behavior strikingly similar to that observed in SSMO thin film (Fig. 1b). The bias dependence of MR%, defined as $\frac{R-R_{LR}}{R_{LR}} \times 100\%$, where R is the measured resistance and R_{LR} denotes the low-resistance state at high magnetic field, is presented in Fig. 3c based on data from Fig .3a, b. Once the applied current exceeds the critical threshold, MR% saturates to ~200% and shows minimal variation with increasing bias.

A similar current-dependent transition is observed under positive bias conditions (Fig. S7). The evolution of MR with bias in our devices differs markedly from the behavior typically reported in conventional magnetic tunnel junctions (MTJs)[42] and SFTJs[28,43]. Conventional SFTJs typically display a bias dependence wherein the MR% initially increases, reaches a peak, and subsequently decreases with further bias[28,44], while in standard MTJs, the MR% generally decreases monotonically with bias[40]. Further insight into the unconventional behavior we observed in our devices is provided by the junction resistance vs. applied current characteristics (Fig. 3d), which reveal an abrupt switching event near −88 μA, from low-resistance state (R_{Low}) to high-resistance state (R_{High}). This switching current coincides with the critical threshold at which the unconventional MR response emerges in the device. Additionally, the magnetic switching field (H_s), defined as in Fig. 2e, exhibits a pronounced increase with the applied current once the critical threshold is exceeded. The magnitude of this effect is quantified by plotting the ΔH_s as a function of ΔI, where ΔH_s represent the change in the switching field with respect to the applied current above the critical current I_C(Fig. 3e). Both switching fields, ΔH_{s1} and ΔH_{s2}, increase linearly with ΔI, suggesting a competitive interaction between the magnetic field-driven alignment of the spins and the

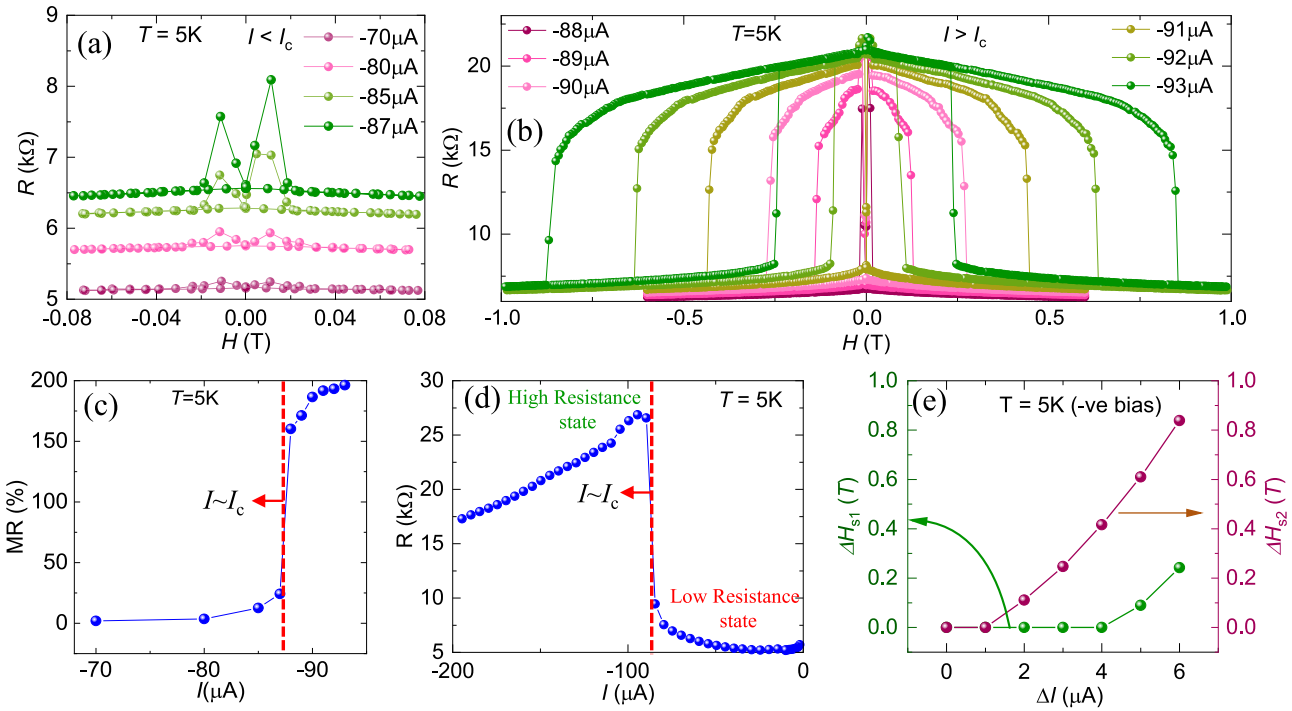

Fig. 3 | Bias-dependent magnetoresistance in spin-filter tunnel junction (SFTJ) devices. a, **b** Magnetoresistance (MR) profiles of the SFTJ device measured at 5 K under various negative bias currents, revealing a pronounced transition in resistance behavior at and above a threshold current of −88 μA ($I \geq I_c$). **c** Extracted MR ratio as a function of applied current, showing a sharp increase in MR up to ~200% beyond the critical current, indicative of strong current-driven phase modulation. **d** Resistance–current (R–I) characteristics under negative bias, confirming abrupt switching associated with a non-equilibrium phase transition. **e** Change in switching field (ΔHs) as a function of excess current above the critical current ($\Delta I = I - I_c$), reflecting the interplay between current-induced magnetic reordering and external magnetic field.

current-induced modification of the magnetic state within the SSMO-FI barrier.

Figure4a presents the R–I characteristics for a representative device with the stack configuration LNO (200 nm)/SSMO (6.5 nm)/STO (1 nm)/LSMO (200 nm), measured at various temperatures. The device exhibits qualitatively distinct transport behavior in the temperature regimes above and below T_C (~100 K), of the SSMO-FI barrier. At 150 K, well above the T_C, the resistance decreases smoothly and exponentially with increasing bias, consistent with a conventional tunnel junction. In contrast, at 5 K, the device displays a pronounced two-state resistance behavior, characterized by an abrupt transition from a low-resistance to a high-resistance state at a threshold current of approximately 20 μA. Notably, comparable unconventional switching behavior is consistently observed across other SSMO-based SFTJ devices with varying device area (Fig. S8). The magnitude of the resistance changes between the low-resistance R_{Low} and high-resistance R_{High} states matches well with the ΔR% values extracted from field-dependent measurements performed at the currents exceeding I_C(see Fig. S9). In contrast, for currents below I_C, the device exhibits a conventional magnetoresistance response characteristic of a quasi-spin-filter tunnel junction[45,46] (see Figs. S7, S9). The unconventional two-state switching behavior persists up to approximately 100 K, with the critical current decreasing monotonically as the temperature increases (Fig. 4a, inset). These observations suggest that such two-state switching arises from current-driven manipulation of magnetic ordering within the barrier layer of the SFTJ devices[47]. The reduction of I_C with temperature suggests that the current-induced magnetic reordering within the SSMO-FI barrier requires progressively lower currents at higher temperatures, as thermal fluctuations weaken the intrinsic ferromagnetic order. The current-induced control of magnetic order within the FI barrier is further supported by temperature-dependent junction resistance measurements (Fig. S10). At bias currents below I_C, the device exhibits typical spin-filter tunnel junction behavior, with resistance decreasing as the temperature drops below T_C[39], reflecting the presence of ferromagnetic order in the barrier layer. In contrast, when measured at currents exceeding I_C, the expected low-temperature resistance drop is absent, consistent with a suppression of ferromagnetic order within the barrier due to an electrically driven phase transition.

The temperature dependence of the current-induced switching is further quantified in Fig. 4b, which presents the variation of ΔR%, defined as the change in the device resistance at the critical current I_C, as a function of temperature. With increasing temperature, ΔR% decreases monotonically, approaching zero near 100 K, which coincides with the T_C of the SSMO-FI barrier layer. This trend mirrors the temperature-dependent ΔR% behavior extracted from field-dependent measurements (Fig. S9d), reinforcing the conclusion that the two-state resistance switching is directly linked to the magnetic ordering within the barrier. A similar temperature-dependent MR behavior is also observed in devices with an 8.5nm-thick SSMO-FI barrier layer (Fig.S7d). We further explored the effect of an external magnetic field on the current-driven switching behavior. Figure4c shows the resistance as a function of applied current for different magnetic fields under negative bias. The switching current exhibits a strong dependence on the applied field, increasing systematically as the magnetic field is raised. This observation points to a competition between the external field, which stabilizes the FM state, and the electrical current, which drives the system toward an AFM phase. The nearly linear relationship between the critical current and the applied field is shown in the inset of Fig. 4c, consistent with trends observed in the MR characteristics (Fig. 3e).

In our devices, when the applied current remains below the critical threshold ($I < I_C$), the SSMO-FI barrier resides in an FM insulating state, characterized by spin-split conduction bands. This spin-splitting

https://doi.org/10.1038/s41467-026-75886-w

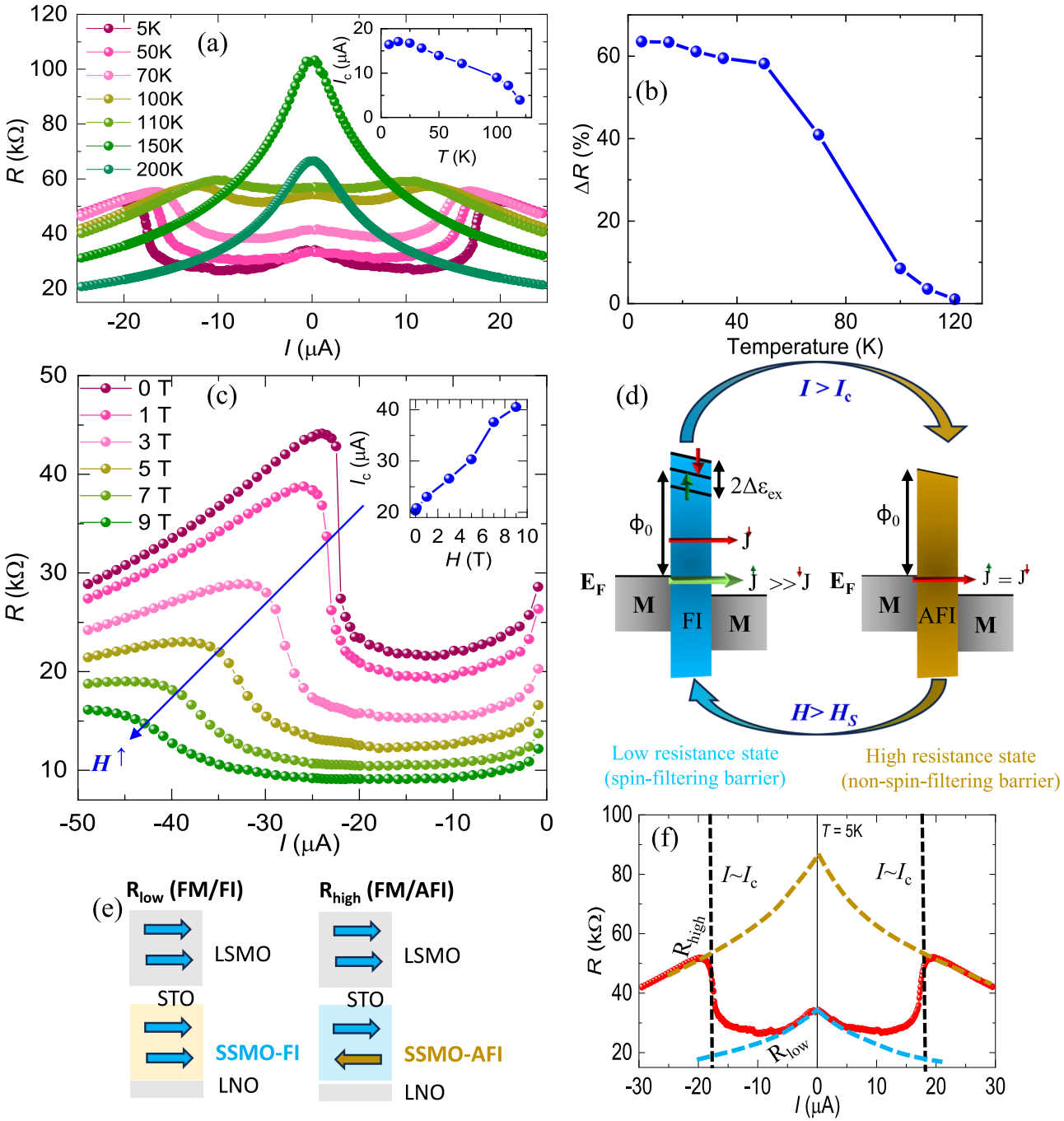

Fig. 4 | Temperature and magnetic field dependence of current-induced resistance switching in SFTJ devices. a Resistance–current (R–I) characteristics measured at various temperatures, showing a clear reduction in the critical switching current (I_C) with increasing temperature (inset), consistent with thermal weakening of ferromagnetic order. **b** Temperature dependence of the current-induced resistance change (ΔR), mirroring the magnetization–temperature (M–T) profile of the SSMO barrier, highlighting the central role of the barrier's magnetic properties in governing switching behavior. **c** R–I curves under different applied magnetic fields, demonstrating a field-dependent shift in I_C. The inset reveals a near-linear relationship between the critical current and magnetic field, suggesting a competition between magnetic field stabilization of the ferromagnetic phase and current-driven destabilization. **d** Schematic illustration of spin-dependent tunneling profiles across the SSMO-FI barrier in a metal(M)/SSMO-FI/metal(M) structure under different current regimes. Below the critical current ($I < I_C$), the ferromagnetic insulating (FI) state exhibits spin-filtering behavior with asymmetric barrier height for spin-up electrons ($\phi_{Low} = \phi_0 - \Delta\varepsilon_{ex}$) where ϕ_0 is the barrier height in the absence of spin splitting. When $I > I_C$, the SSMO-FI transitions into an antiferromagnetic insulating (AFI) state, resulting in a symmetric, higher barrier ($\phi_{High} = \phi_0$) for both spin channels. $J^{\uparrow}$ and $J^{\downarrow}$ denote the current densities carried by majority and minority spins, respectively. **e** Schematic representation of the magnetic configuration of LSMO/STO/SSMO-FI heterostructures for the low-resistance and the high-resistance states. **f** Experimental R–I characteristics for an SFTJ device measured at 5 K, showing a sharp transition near ±20 μA (I_C). The dotted golden line denotes extrapolated R–I responses for the AFI phases with corresponding higher barrier heights, whereas the dotted blue line represents the extrapolated R–I response for the FI phases corresponding to the lower barrier height.

results in distinct barrier heights for electrons with different spin orientations, reducing the barrier for one spin channel (e.g., spin-up) while increasing it for the other (e.g., spin-down), as illustrated schematically in Fig. 4d. However, upon exceeding the I_C, the SSMO-FI barrier undergoes a transition to an AFM state, analogous to a conventional tunnel barrier without spin-split contributions. The transition between low and high-resistance states in the device is governed by the corresponding change in the effective barrier height of the SSMO-FI layer. For applied currents below the I_C, the barrier resides in a FI state, with preferential spin-polarized tunneling determined by the reduced effective barrier height, given by $\phi_{Low} = \phi_O - \Delta\varepsilon_{ex}$, where ϕ_O is the average barrier height and $2\Delta\varepsilon_{ex}$ represents the exchange splitting of the conduction band. When the applied current exceeds I_c, the spin-splitting vanishes as the system transitions to an AFM insulating state, resulting in an increased barrier height of $\phi_{High} = \phi_O$. This abrupt increase in the tunneling barrier gives rise to a sharp transition to a high-resistance state.

To elucidate the underlying mechanism and provide a qualitative consistency check for our observations, we developed a unified, multi-scale theoretical framework (see Supplementary Information for details). At the microscopic electronic level, our model based on the Hubbard Hamiltonian combined with the non-equilibrium Green's function (NEGF) formalism captures both the resistance switching and the evolution of magnetic order (see Supplementary Information, Fig. S12 and Section B). This provides qualitative theoretical support for the interpretation that the electrically driven high-resistance state originates from suppression of ferromagnetism and stabilization of an antiferromagnetic-like configuration in the barrier under nonequilibrium conditions. The observed current-induced FM-to-AFM phase transition is consistent with an inverse metamagnetic transition[25,26], which can be reversed by applying a sufficiently large magnetic field ($H > H_s$), as schematically illustrated in Fig. 4d. The corresponding magnetic configurations of the LSMO/STO/SSMO-FI film stack for the FM/FI and FM/AFI states produce the R_{Low} and R_{High} states, respectively, as summarized in Fig. 4e. To further bridge this microscopic magnetic transition to the mesoscopic device transport, we applied a single-band tight-binding approach combined with the NEGF formalism (see Supplementary Information, Fig. S13 and Section C). This component of the framework shows, at a phenomenological level, that the two distinct resistance states in the R–I characteristics can be correlated with tunneling across the two effective barrier heights ϕ_{Low} and ϕ_{High}, as shown by the dotted lines in the experimental R–I plot measured at 5 K (Fig. 4f). Finally, extending our framework to macroscopic dynamics, the unique MR behavior observed above I_C is qualitatively reproduced by incorporating microspin dynamics simulations into the tight-binding transport model (see Supplementary Information, Fig. S14 and Section D). Through this integrated approach, we also verified that spin-transfer torque (STT) alone is insufficient to achieve the switching in our device solely through current-induced torque (see Supplementary Information, Fig. S15 and Section E). While STT may contribute to the overall dynamics, our unified framework establishes that the dominant mechanism in our system arises from the electrically driven inverse metamagnetic transition, a fundamentally distinct phenomenon in spintronic devices.

In summary, we report the experimental realization and theoretical understanding of a current-induced inverse metamagnetic transition in the correlated oxide $Sm_{1-x}Sr_xMnO_3$. Our results demonstrate that applying a critical current to epitaxial thin films of SSMO drives a robust, reversible transition from a ferromagnetic state to an antiferromagnetic-like phase, accompanied by dramatic resistance switching, orbital reordering, and the collapse of long-range ferromagnetic ordering. This phenomenon, verified through XMCD/XLD measurements, represents a fundamentally distinct mode of electrically driven magnetic phase control distinct from conventional spin-transfer or spin-orbit torque mechanisms. By engineering a ferromagnetic insulating phase of SSMO and integrating it into nanoscale spin-filter tunnel junctions, we successfully realize this inverse metamagnetic transition in a device context, enabling giant, hysteretic magnetoresistance with strong bias and temperature dependence. Our findings establish a phase-transition-based paradigm for non-equilibrium spintronic functionality in complex oxides and open the door to energy-efficient memory and logic technologies based on current-controlled magnetic phase transitions.

Methods

Materials growth

All oxide films, $Sm_{0.6}Sr_{0.4}MnO_3$ (SSMO), $Sm_{0.75}Sr_{0.25}MnO_3$ (SSMO-FI), STO ($SrTiO_3$), LNO ($LaNiO_3$), and LSMO ($La_{0.7}Sr_{0.3}MnO_3$), along with their heterostructures, were epitaxially grown on STO (001) single-crystal substrates utilizing pulsed laser deposition (PLD). The growth process employed a KrF excimer laser (wavelength = 248 nm) at a 5 Hz repetition rate and a fluence of approximately 1 J cm^{-2}, targeting stoichiometric ceramic sources. The deposition conditions were finely controlled, with O_2 partial pressure set to 20 Pa for manganite (SSMO and LSMO) and STO films, while maintaining the substrate temperature at 700 °C. In contrast, LNO films required a slightly different environment, with an N_2O partial pressure of 30 Pa and a reduced substrate temperature of 650 °C. Post-deposition, the samples underwent a gradual cooling phase to room temperature in an atmosphere of 100 Pa N_2O, ensuring structural stability and crystallinity.

Structural characterization

The phase and crystalline quality of the deposited films were rigorously evaluated using a Rigaku Smart Lab high-resolution X-ray diffractometer equipped with Cu K_α radiation, a two-bounce hybrid monochromator, and a 0.5 mm slit beam tunnel. This comprehensive analysis provided critical insights into the epitaxial nature and structural integrity of the multilayer films.

XAS, XLD, and XMCD measurements

The in-situ electric current-dependent X-ray absorption spectroscopy (XAS), X-ray linear dichroism (XLD), and X-ray magnetic circular dichroism (XMCD) measurements were performed at the Mn $L_{3,2}$-edges at the DEIMOS beamline, Soleil synchrotron, Paris, France. All measurements were conducted in total fluorescence yield (TFY) mode by recording the fluorescence from the sample with absorbing X-ray, providing comparatively bulk-sensitive information (~100 nm from the top of the sample surface). The experiments were carried out at 25 K to probe the low-temperature electronic, orbital, and magnetic states. For the XMCD measurements, a magnetic field of 1 T was applied through an electromagnet, the orientation of which was fixed, and the circular polarization of the incident beam was altered by adjusting the undulator shifts. The applied magnetic field was parallel to the incident beam and had a grazing incidence to the sample surface (20°) (See inset of Fig. 1c). Similarly, for the XLD measurements, the linear polarization of the incident beam was altered between linear horizontal (LH) and linear-vertical (LV) by adjusting the undulator shifts. In the grazing incidence geometry, LH and LV give the I_c and I_{ab} signals, respectively. The experimental geometry for the XLD measurement is schematically illustrated in the inset of Fig. 1d. When the electric field vector **E** of the beam is parallel to the sample surface, the resulting spectrum provides information on the in-plane orbitals, i.e., x^2-y^2 & xy orbitals, which is denoted as I_{ab}. Conversely, when **E** is an oblique angle to the sample surface, the spectrum predominantly reflects the out-of-plane orbitals, i.e., $3z^2$-r^2, yz, and zx orbitals, referred to as I_c. The XLD signal, defined as the difference (I_{ab}-I_c), reveals the orbital polarization: a positive signal indicates an out-of-plane (c-axis) orbital polarization, while a negative signal reflects an in-plane (ab-plane) orbital polarization. To support the interpretation of the XLD line shape in terms of Mn orbital polarization, charge-transfer multiplet calculations were

performed for Mn^{3+} using CTM4XAS within a ligand-field framework[48], as described in Supplementary Information, Section A.

Transmission electron microscopy imaging

The electron transparent TEM-lamella was prepared using a dual beam SEM/ FIB instrument (Scios Nanolab, ThermoFisher) with Ga^+ ions at currents varying from 0.3 nA to 50 pA. The acceleration voltage was kept at 30 kV. The final cleaning was performed at 2 kV to remove the Ga^+ damage regions. The HR-STEM imaging and energy dispersive spectroscopy (EDS) mapping were conducted in an aberration-probe-corrected TEM (Titan Themis, ThermoFisher) in STEM mode, equipped with a Super-X-ray EDS detector. The STEM images with atomic resolution were captured using Velox software (ThermoFisher) with a drift-compensated frame integration (DCFI) process and a high-angle annular dark-field (HAADF) detector. The camera length was set to 160 mm, and the probe current was kept 0.08 nA.

Device fabrication

The multilayer epitaxial oxide thin films were first prepared for device integration. A polycrystalline gold layer, approximately 200 nm thick, was uniformly deposited on the films via DC magnetron sputtering. This layer serves a dual function: acting as a top contact and offering protection against ion-beam damage during subsequent processing. Device patterning was initiated by conventional optical photolithography, delineating a series of 4-µm-wide tracks. These tracks were then precisely etched using Ar-ion milling. The final step involved focused ion beam (FIB) nanomachining, which meticulously sculpted the nanopillar devices, each with average dimensions of 250 nm × 250 nm. Both the top (LNO) and bottom (LSMO) metallic electrode layers were maintained at a thickness of approximately 200 nm. Each device in a chip is connected to four large-area contact pads, facilitating four-point transport measurements.

Magnetic and transport measurements

Magnetization measurements were conducted using a SQUID magnetometer from Quantum Design in an in-plane configuration. The resistance switching field of the fabricated devices was compared to the coercive field of the SSMO and LSMO layers, as determined by the M-H data of these individual layers. The electrical properties of the devices were rigorously evaluated using a four-probe current-biased setup within a pulse-tube cryocooled measurement system. The device was wire-bonded with a 20-pin chip carrier, ensuring a robust electrical conducting path. This configuration ensures that the current flows from the Au-LNO top electrode layer to the bottom ferromagnetic metallic LSMO layer via the SSMO and STO tunnel barrier layers. The bias direction is defined with respect to the top electrode, such that the negative bias corresponds to current flows from the LNO top electrode to the LSMO bottom electrode

Data availability

Source data is included with this paper. All other data that support the findings of this study are available from the corresponding authors upon request. Source data are provided with this paper.

References

1. Matsukura, F., Tokura, Y. & Ohno, H. Control of magnetism by electric fields. *Nat. Nanotechnol.* **10**, 209–220 (2015).
2. Cherifi, R. O. et al. Electric-field control of magnetic order above room temperature. *Nat. Mater.* **13**, 345–351 (2014).
3. Ramesh, R. & Manipatruni, S. Electric field control of magnetism. Proc. R. Soc. A: Math. Phys. Eng. Sci. **477**, (2021).
4. Fert, A., Ramesh, R., Garcia, V., Casanova, F. & Bibes, M. Electrical control of magnetism by electric field and current-induced torques. *Rev. Mod. Phys.* **96**, 1–78 (2024).
5. Dieny, B. et al. Opportunities and challenges for spintronics in the microelectronics industry. *Nat. Electron.* **3**, 446–459 (2020).
6. Wolf, S. A. et al. Spintronics: a spin-based electronics vision for the future. *Science* **294**, 1488–1495 (2001).
7. Bibes, M. & Barthélémy, A. Oxide spintronics. *IEEE Trans. Electron Devices* **54**, 1003–1023 (2007).
8. Ji, H. et al. Recent progress on low-power electrical control of magnetization in transition metal oxide heterostructures. *Adv. Funct. Mater.* **2505227**, 1–19 (2025).
9. Chen, H. & Yi, D. Spin-charge conversion in transition metal oxides. *APL Mater.* **9**, 060908 (2021).
10. Wang, Q., Gu, Y., Chen, C., Pan, F. & Song, C. Oxide spintronics as a knot of physics and chemistry: recent progress and opportunities. *J. Phys. Chem. Lett.* **13**, 10065–10075 (2022).
11. Han, Y. et al. Transition metal oxides: a new frontier in spintronics driven by novel quantum states and efficient charge-spin interconversion. *Front. Mater.* **11**, 1–22 (2024).
12. Roy, S. B., Chaddah, P., Pecharsky, V. K. & Gschneidner, K. A. Overview no. 145 metamagnetic transitions, phase coexistence and metastability in functional magnetic materials. *Acta Mater.* **56**, 5895–5906 (2008).
13. Marín Ramírez, J. M. et al. Experimental exploration of dynamic phase transitions and associated metamagnetic fluctuations for materials with different Curie temperatures. *Phys. Rev. E* **102**, 1–12 (2020).
14. Ranaut, D. et al. Low-temperature thermodynamics of metamagnetism in insulating DyVO4. *Phys. Rev. B* **111**, 1–7 (2025).
15. Cenker, J. et al. Reversible strain-induced magnetic phase transition in a van der Waals magnet. *Nat. Nanotechnol.* **17**, 256–261 (2022).
16. Kuwahara, H., Tomioka, Y., Asamitsu, A., Moritomo, Y. & Tokura, Y. A first-order phase transition induced by a magnetic field. *Science* **270**, 961–963 (1995).
17. Sokolov, D. A. et al. Metamagnetic texture in a polar antiferromagnet. *Nat. Phys.* **15**, 671–677 (2019).
18. Tang, N. et al. Spin–orbital liquid state and liquid–gas metamagnetic transition on a pyrochlore lattice. *Nat. Phys.* **19**, 92–98 (2023).
19. Pressacco, F. et al. Subpicosecond metamagnetic phase transition in FeRh driven by non-equilibrium electron dynamics. *Nat. Commun.* **12**, 1–8 (2021).
20. Nan, T. et al. Electric-field control of spin dynamics during magnetic phase transitions. *Sci. Adv.* **6**, 1–6 (2020).
21. Worledge, D. C. & Hu, G. Spin-transfer torque magnetoresistive random access memory technology status and future directions. *Nat. Rev. Electr. Eng.* **1**, 730–747 (2024).
22. Kim, K.-W., Park, B.-G. & Lee, K.-J. Spin current and spin-orbit torque induced by ferromagnets. *npj Spintronics* **2**, 1–8 (2024).
23. Na, T., Kang, S. H. & Jung, S. O. STT-MRAM sensing: a review. *IEEE Trans. Circuits Syst. II: Exp. Briefs* **68**, 12–18 (2021).
24. Shao, Q. et al. Roadmap of spin-orbit torques. *IEEE Trans. Magn.* **57**, (2021).
25. Kainuma, R. et al. Magnetic-field-induced shape recovery by reverse phase transformation. *Nature* **439**, 957–960 (2006).
26. Hauser, R. et al. Decoupling of the magnetic ordering of the rare-earth and the Co sublattice in Er1-xYxCo2 compounds driven by substitution or pressure. *Phys. Rev. B Condens. Matter Mater. Phys.* **61**, 1198–1210 (2000).
27. Moodera, J. S., Meservey, R. & Hao, X. Variation of the electron-spin polarization in EuSe tunnel junctions from zero to near 100% in a magnetic field. *Phys. Rev. Lett.* **70**, 853–856 (1993).
28. Prasad, B., Zhang, W., Jian, J., Wang, H. & Blamire, M. G. Strongly bias-dependent tunnel magnetoresistance in manganite spin filter tunnel junctions. *Adv. Mater.* **27**, 3079–3084 (2015).
29. Srivastava, M. K., Singh, M. P., Kaur, A., Razavi, F. S. & Singh, H. K. Low-field anisotropic colossal magnetoresistance in $Sm_{0.53}Sr_{0.47}MnO_3$ thin films. *J. Appl. Phys.* **110**, 0–5 (2011).

30. Tokura, Y. & Nagaosa, N. Orbital physics in transition-metal oxides. *Science* **288**, 462–468 (2000).
31. Tebano, A. et al. Evidence of orbital reconstruction at interfaces in ultrathin $La_{0.67}Sr_{0.33}MnO_3$ films. *Phys. Rev. Lett.* **100**, 2–5 (2008).
32. Fang, Z., Solovyev, I. V. & Terakura, K. Phase diagram of tetragonal manganites. *Phys. Rev. Lett.* **84**, 3169–3172 (2000).
33. Konishi, Y. et al. Orbital-state-mediated phase-control of manganites. *J. Phys. Soc. Jpn.* **68**, 3790–3793 (1999).
34. Chowdhury, S. et al. Electronic, orbital, and spin reconstructions at the interface between metallic $La_{0.7}Sr_{0.3}MnO_3$ and charge-disproportionated insulator $SrCoO_{2.5}$. *J. Phys. Chem. C.* **125**, 17537–17545 (2021).
35. Aruta, C. et al. Orbital occupation, atomic moments, and magnetic ordering at interfaces of manganite thin films. *Phys. Rev. B Condens. Matter Mater. Phys.* **80**, 014431 (2009).
36. Keshri, A. et al. Orbital and spin reconstruction by interface symmetry engineering in oxide superlattices. *Small* **21**, e2500089 (2025).
37. Nagahama, T., Santos, T. S. & Moodera, J. S. Enhanced magnetotransport at high bias in quasimagnetic tunnel junctions with EuS spin-filter barriers. *Phys. Rev. Lett.* **99**, 016602 (2007).
38. Gajek, M. et al. Spin filtering through ferromagnetic BiMnO3 tunnel barriers. *Phys. Rev. B* **72**, 020406 (2005).
39. Moodera, J. S., Santos, T. S. & Nagahama, T. The phenomena of spin-filter tunnelling. *Journal of Physics Condensed Matter* **19**, (2007).
40. Moodera, J. S., Nowak, J. & Van De Veerdonk, R. J. M. Interface magnetism and spin wave scattering in ferromagnet-insulator-ferromagnet tunnel junctions. *Phys. Rev. Lett.* **80**, 2941–2944 (1998).
41. Ramos, A. et al. Room temperature spin filtering in epitaxial cobalt-ferrite tunnel barriers. *Appl. Phys. Lett.* **91**, 122107 (2007).
42. Ikeda, S. et al. A perpendicular-anisotropy CoFeB–MgO magnetic tunnel junction. *Nat. Mater. 2010* **9**, 721–724 (2010).
43. Harada, T. et al. Large tunnel magnetoresistance in epitaxial oxide spin-filter tunnel junctions. *Adv. Funct. Mater.* **22**, 4471–4475 (2012).
44. Miao, G. X., Chang, J., Assaf, B. A., Heiman, D. & Moodera, J. S. Spin regulation in composite spin-filter barrier devices. *Nat. Commun.* **5**, 3682 (2014).
45. Gajek, M. et al. Tunnel junctions with multiferroic barriers. *Nat. Mater. 2007* **6**, 296–302 (2007).
46. Harada, T. et al. Spin-filter tunnel junction with matched Fermi surfaces. *Phys. Rev. Lett.* **109**, 3–7 (2012).
47. Kurbakov, A. I. Electronic, structural and magnetic phase diagram of Sm1-xSrxMnO3 manganites. *J. Magn. Magn. Mater.* **322**, 967–972 (2010).
48. Stavitski, E. & de Groot, F. M. F. The CTM4XAS program for EELS and XAS spectral shape analysis of transition metal L edges. *Micron* **41**, 687–694 (2010).

Acknowledgments

S. M. is thankful to DST for providing the INSPIRE fellowship. V. K. acknowledges support from SERB (File No. PDF/2022/000528) for the National Post-Doctoral Fellowship (NPDF). S.M. and V. K. acknowledge the fabrication, characterization, and measurement facilities at the Center for Nanoscience and Engineering (CeNSE), IISc. A. G. and S. K. M. acknowledge the Advanced Facility for Microscopy and Microanalysis (AFMM), IISc. Philippe Ohresser is acknowledged for helping during synchrotron measurements.

Author contributions

B.P. has designed the experiments. B.P., S.M., V.K. and A.K.M. carried out materials synthesis, characterization, device fabrication, and measurements. S.C., S.N., J.K.D. and G.P. have performed the synchrotron experiment. S.C. performed the charge transfer multiplet simulations. A.K. and S.M. performed the atomistic simulations, and W.S.T. and Y.H.T. did the tight-binding and microspin dynamics simulations. A.G., S.K.M., and J.M. performed the HR-TEM. A.G. and S.K.M. performed EDX. B.P., S.M., V.K., M.B., A.O., A.K., A.M., M.B. and Y.H.T. contributed to analyzing data and writing the manuscript. All authors discussed the results and commented on the manuscript.

Funding

B.P. discloses the funding from IISc (startup grant), the Ministry of Education (STARS, Grant No. MoE-STARS/STARS-2/2023-0496), the Science and Engineering Research Board (SERB) (Grant No. CRG/2022/002830), and CEFIPRA (Project No. 6908-1). Y.H.T. also discloses financial support from the National Science and Technology Council, Taiwan (NSTC 112-2112-M-008-036).

Competing interests

The authors declare no competing interests.

Additional information

Supplementary information The online version contains supplementary material available at https://doi.org/10.1038/s41467-026-75886-w.

Correspondence and requests for materials should be addressed to Bhagwati Prasad.

Peer review information *Nature Communications* thanks the anonymous reviewers for their contribution to the peer review of this work. A peer review file is available.